

14 GHz Schottky Diodes Using a *p*-Doped Organic Polymer

Kalaivanan Loganathan, Alberto D. Scaccabarozzi, Hendrik Faber, Federico Ferrari, Zhanibek Bizak, Emre Yengel, Dipti R. Naphade, Murali Gedda, Qiao He, Olga Solomeshch, Begimai Adilbekova, Emre Yarali, Leonidas Tsetseris, Khaled N. Salama, Martin Heeney, Nir Tessler, and Thomas D. Anthopoulos*

The low carrier mobility of organic semiconductors and the high parasitic resistance and capacitance often encountered in conventional organic Schottky diodes hinder their deployment in emerging radio frequency (RF) electronics. Here, these limitations are overcome by combining self-aligned asymmetric nanogap electrodes (≈ 25 nm) produced by adhesion lithography, with a high mobility organic semiconductor, and RF Schottky diodes able to operate in the 5G frequency spectrum are demonstrated. C_{16} IDT-BT is used, as the high hole mobility polymer, and the impact of *p*-doping on the diode performance is studied. Pristine C_{16} IDT-BT-based diodes exhibit maximum intrinsic and extrinsic cutoff frequencies (f_c) of >100 and 6 GHz, respectively. This extraordinary performance is attributed to the planar nature of the nanogap channel and the diode's small junction capacitance (<2 pF). Doping of C_{16} IDT-BT with the molecular *p*-dopant $C_{60}F_{48}$ improves the diode's performance further by reducing the series resistance resulting to intrinsic and extrinsic f_c of >100 and ≈ 14 GHz respectively, while the DC output voltage of an RF rectifier circuit increases by a tenfold. Our work highlights the importance of the planar nanogap architecture and paves the way for the use of organic Schottky diodes in large-area RF electronics of the future.

while radio frequency (RF) wireless energy harvesting (RF-WEH) is considered one of the most viable solutions for powering these distributed devices.^[3] The central component that determines the frequency of operation and the power conversion efficiency of RF-WEH systems is the rectifier unit.^[4] State-of-the-art rectifiers are based on Schottky diodes made from Si-CMOS and III–V semiconductor technologies.^[5] Unfortunately, these technologies are characterized by limited mechanical compliance and rely on costly processing methods. An alternative option is to use organic semiconductors that are simple to process on a wide range of substrate materials using up-scalable printing techniques.^[6] Unfortunately, to date the deployment of organic semiconductors in rectifier circuits is hindered by their relatively low operating frequency (f_c) given by^[1,7]

$$f_c = \frac{1}{2\pi R_s C_j} \quad (1)$$

1. Introduction

The continuing commercial success of the Internet-of-Things (IoT) device ecosystem requires implementation of emerging mobile communication technologies, such as 5G and 6G, and the development of means to reliably produce and power billions of devices.^[1,2] For instance, inexpensive mass manufacturing strategies are key for the massive deployment of IoT sensor nodes,

where R_s is the series resistance and C_j is the junction capacitance of the diode. For conventional sandwich organic diode architectures, these parameters are always relatively high, ultimately limiting the frequency response of the device. In order to overcome these limitations, the development of advanced diode architectures and improved material formulations with enhanced charge mobility is urgently required.


K. Loganathan, A. D. Scaccabarozzi, H. Faber, F. Ferrari, E. Yengel, D. R. Naphade, M. Gedda, B. Adilbekova, E. Yarali, T. D. Anthopoulos
King Abdullah University of Science and Technology (KAUST)
KAUST Solar Center (KSC)
Thuwal 23955-6900, Saudi Arabia
E-mail: thomas.anthopoulos@kaust.edu.sa

Z. Bizak, K. N. Salama
King Abdullah University of Science and Technology (KAUST)
Computer, Electrical and Mathematical Sciences and Engineering (CEMSE)
Advanced Membranes and Porous Materials Center (AMPM)
Thuwal 23955-6900, Saudi Arabia

Q. He, M. Heeney
Department of Chemistry and Centre for Processable Electronics
Imperial College London
London W12 0BZ, UK

O. Solomeshch, N. Tessler
The Zisapel Nano-Electronic Center
Department of Electrical Engineering
Technion-Israel Institute of Technology
Haifa 3200, Israel

L. Tsetseris
Department of Physics
National Technical University of Athens
Athens GR-15780, Greece

 The ORCID identification number(s) for the author(s) of this article can be found under <https://doi.org/10.1002/adma.202108524>.

DOI: 10.1002/adma.202108524

Here, we used adhesion lithography (a-Lith)^[8] to fabricate self-aligned, asymmetric (Al, Au) planar metal electrodes separated by a ≤ 25 nm nanogap. The advantageous co-planar electrode architecture yields devices with low capacitance ($< \text{pF}$), which is a prerequisite for high-frequency operation.^[9] To test this hypothesis we combined the self-aligned nanogap electrodes with a high mobility poly(indacenodithiophene-co-benzothiadiazole) ($\text{C}_{16}\text{IDT-BT}$) organic semiconductor to produce planar *p*-type Schottky diodes, where Au and Al provide the Ohmic and rectifying contacts, respectively. The ensuing diodes were found to exhibit exceptionally high intrinsic and extrinsic frequencies of > 100 GHz and 6 GHz, outperforming all previously reported organic diodes. We also investigated the impact of *p*-doping the $\text{C}_{16}\text{IDT-BT}$ with $\text{C}_{60}\text{F}_{48}$, and showed that optimal doping results to a record extrinsic cutoff frequency of ≈ 14 GHz and to a tenfold improvement of the direct current (DC) output voltage of rectifier circuits.

2. Results and Discussion

Figure 1a depicts the a-Lith steps used to manufacture the self-aligned asymmetric electrode nanogaps on wafer scale, while **Figure S1** (Supporting Information) presents photographs of the actual wafer at each processing step. Further details of the a-Lith process can be found in the Experimental Section and in our previous publications.^[10–12] In brief, a-Lith relies on the application of a self-assembled monolayer (SAM), in this case octadecyl phosphonic acid (ODPA), onto the surface of the

lightly oxidized first metal electrode (M1, i.e., Al). The metallophilic SAM makes the surface of M1 highly hydrophobic which in turn reduces the adhesion with the subsequently deposited second metal electrode (M2), while leaving the substrate's surface unchanged. A peel-off step is then applied to remove (i.e., mechanically delaminate) regions of M2 (Au) overlapping with M1 (Al-SAM) (**Figure 1a**). The remaining SAM present on the surface of M1 can then be removed by exposing the wafer to Ar plasma for a few seconds. The ensuing structures are self-aligned a/symmetric M1–M2 nanogaps of arbitrary shape and size. **Figure 1b** shows a photograph of a 4 inch wafer containing a large number of circular Al–Au nanogap arrays (inset), with the overlapping M1–M2 regions just being removed (mechanically peeled-off) using glue. In these planar diodes, the width (*W*) of the nanogap is defined by the circumference of the inner Au electrode and for this particular experiment was varied from 250 to 5000 μm . **Figure 1c** shows an isolated co-planar Al–Au nanogap device with $W = 500$ μm , while **Figure 1d** displays an SEM image of the nanogap. Estimation of the interelectrode distance (i.e., nanogap) was performed using the method derived from Kano et al.,^[13] and used recently by our group.^[10] **Figure 1e** shows the distribution of the nanogap size extracted from SEM images of five different samples from three different production batches (see **Figure S2**, Supporting Information). The majority peak is centered on a nanogap size of 22.9 nm with a secondary peak at higher values. Variations in gap size are mainly driven by a distribution of metal grain sizes in M1 and M2, with additional factors being the peeling force and direction.^[8,10]

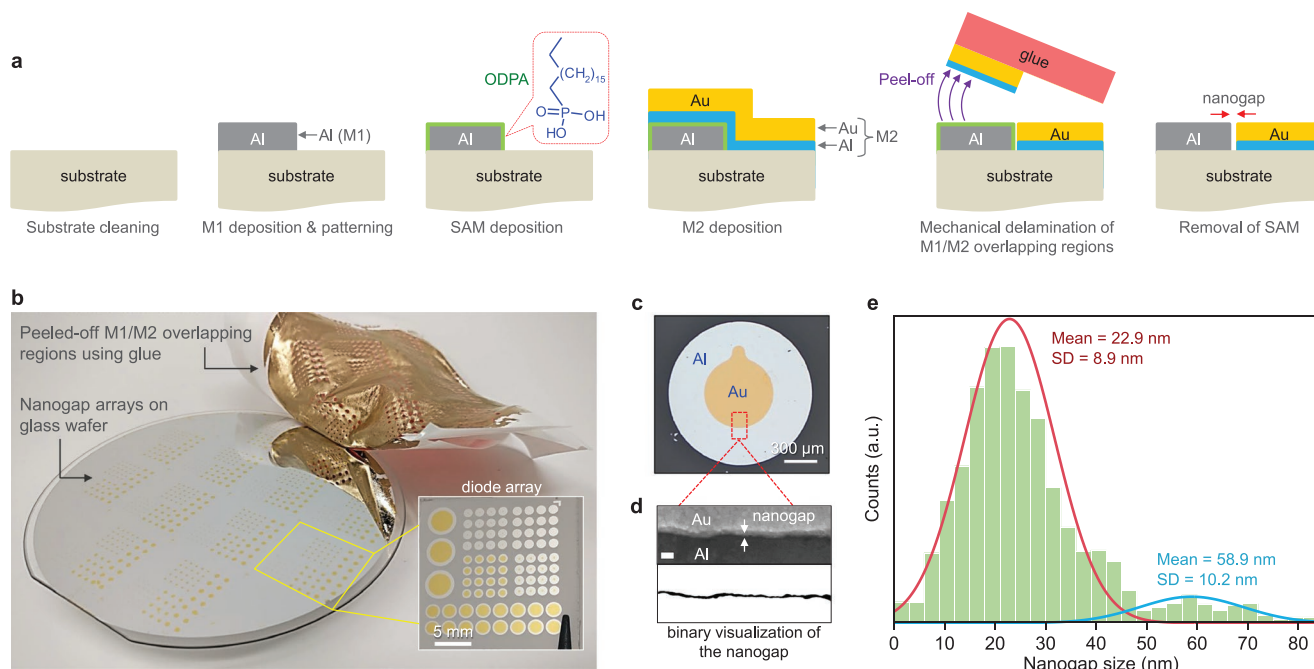


Figure 1. a) Schematic illustrations of the adhesion lithography (a-Lith) process steps. b) A photograph showing the peel-off step and removal of the overlapping regions of the bimetallic M2 electrode (Al–Au) from the surface of M1-SAM electrode across a 4 inch glass wafer. The inset photograph shows a diced chip containing an array of circular, self-aligned planar Al/Al–Au nanogap electrodes. c) A high resolution optical microscope image of a single nanogap device. d) SEM image of the nanogap formed between M1 and M2 and the corresponding binary visualization where only the area within the gap is shown as dark pixels. The scale bar is 100 nm. e) Histogram summarizing the combined nanogap size distribution obtained from five Al/Al–Au SEM images (see **Figure S2**, Supporting Information). The gap size extraction followed a method adapted from Kano et al.^[13]

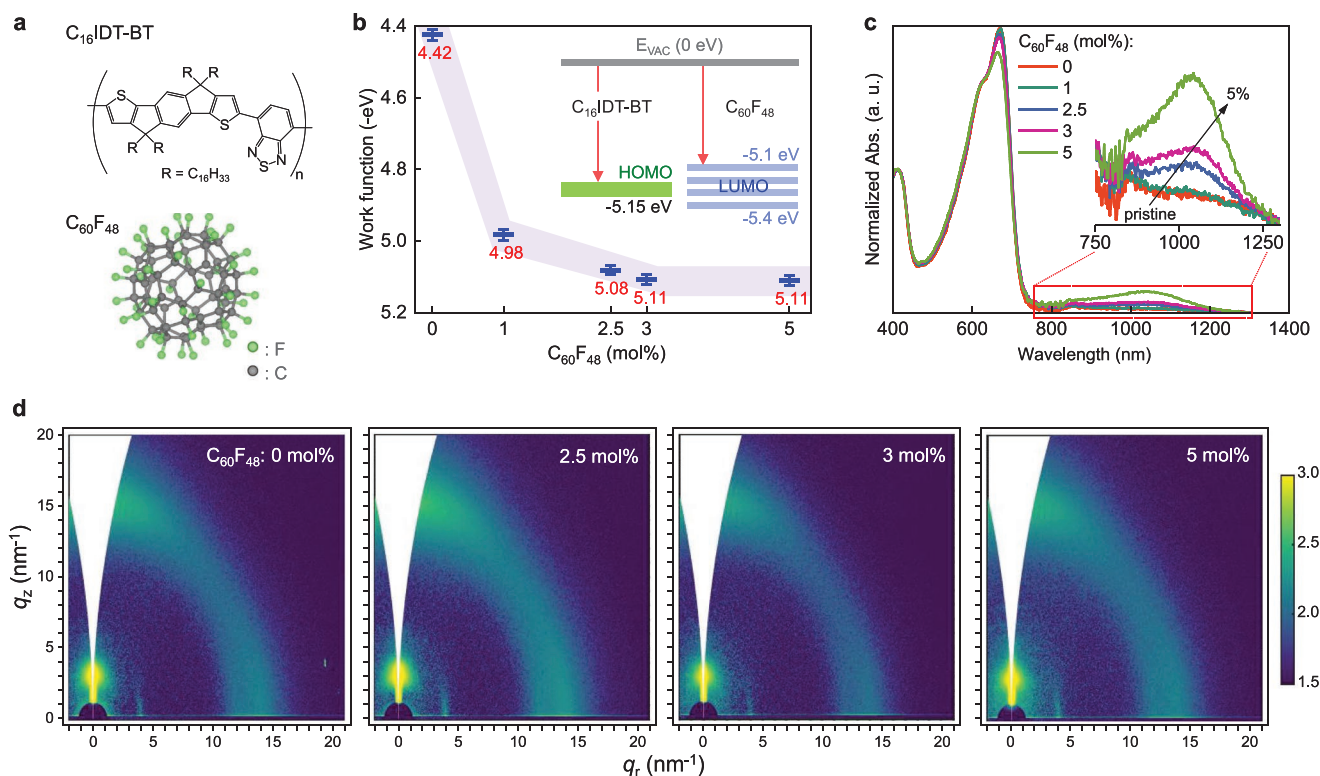


Figure 2. a) Chemical structures of the C₁₆IDT-BT polymer and the molecular *p*-dopant C₆₀F₄₈. b) Evolution of the work function (WF) of C₁₆IDT-BT with dopant concentration measured via Kelvin Probe. For each sample tested the WF was calculated using a cleaned highly oriented pyrolytic graphite (HOPG) sample with a WF of 4.5 eV as the reference electrode. All measurements were performed inside a nitrogen-filled glove box. The inset presents (not in scale) the HOMO and LUMO energy levels for C₁₆IDT-BT^[23] and C₆₀F₄₈.^[37–39] c) Absorption spectra for neat and C₆₀F₄₈ doped C₁₆IDT-BT polymer films. The inset shows the polaron peaks at 1040 nm. d) Grazing incidence wide angle X-ray scattering (GIWAXS) patterns for neat and C₆₀F₄₈-doped C₁₆IDT-BT polymer layers.

Having confirmed a-Lith as a suitable patterning technique for the manufacturing of planar asymmetric electrodes, we identified several conjugated polymers as candidate semiconductors since they combine solution processability and potentially high mobility.^[14–17] Among those the C₁₆IDT-BT polymer (Figure 2a) was chosen since it is known to exhibit superior hole transport properties and low contact resistance with Au electrodes in thin-film transistors (TFTs).^[18–22] Moreover, recent work has demonstrated that *p*-doping of C₁₆IDT-BT can result in improved organic TFTs with reduced contact resistance and record hole mobility.^[14,23–25] To explore the potential of doping the organic semiconductor in Schottky diodes, we utilized the organic semiconductor in Schottky diodes, we utilized the molecular *p*-type dopant C₆₀F₄₈ (Figure 2a) and studied its impact on the operating characteristics of the planar diodes.

We first assessed the ability of C₆₀F₄₈ to *p*-dope C₁₆IDT-BT, since the physical process of charge transfer may be affected by the characteristics of the particular materials involved.^[26] Calibrated Kelvin Probe (KP) measurements (Figure 2b) reveal that the workfunction (WF) in C₁₆IDT-BT increases rapidly upon doping with C₆₀F₄₈ from 4.42 eV (pristine polymer, 0 mol%) to 5.11 eV for 5 mol% doping, where it stabilizes. Further details of the measurements procedures can be found in the Experimental Section. We note that the value of 4.42 eV measured for the pristine C₁₆IDT-BT is very close to the middle of its bandgap (E_G), given as $|HOMO| - (E_G/2) = 5.15 - (1.65/2) = 4.32$ eV

(E_G was estimated from the onset of absorption in Figure 2c), as would be expected for an intrinsic semiconductor. On the other hand, the Fermi energy level (E_F) undergoes a noticeable shift toward the highest occupied molecular orbital (HOMO) of the polymer (5.15 eV, see inset in Figure 2b) upon C₆₀F₄₈ incorporation and plateaus for concentrations >2.5 mol%. This is a characteristic of the *p*-doping process and is attributed to the electron transfer from the HOMO of C₁₆IDT-BT to the lowest unoccupied molecular orbital (LUMO) of C₆₀F₄₈ (inset in Figure 2b), in agreement with previous reports.^[23] The impact of *p*-doping on charge transport in C₁₆IDT-BT was further assessed using field-effect transistor measurements (Figure S3, Supporting Information). The transfer characteristics of C₁₆IDT-BT-based transistors with 2.5 mol% C₆₀F₄₈ exhibit a major increase (2–3 orders of magnitude) in the channel off current (I_{OFF}) accompanied by a characteristic shift in the threshold voltage (V_T) toward zero while the hole mobility remains largely unchanged (≈ 0.6 cm² V^{−1} s^{−1}). Additional experimental evidence of the *p*-doping effect were obtained from ultraviolet–visible (UV–Vis) absorption measurements of C₁₆IDT-BT films before and after doping with C₆₀F₄₈ at concentrations in the range of 1–5 mol% (Figure 2c). From the onset of absorption of the pristine C₁₆IDT-BT film, the optical E_G was estimated yielding a value of ≈ 1.65 eV. All C₆₀F₄₈-doped C₁₆IDT-BT layers exhibit similar onset but with an additional broad polaronic absorption peak

centered at ≈ 1040 nm, which becomes more intense with increasing dopant concentration (inset, Figure 2c), further supporting the *p*-dopant character of $C_{60}F_{48}$.

Grazing incidence wide angle X-ray scattering (GIWAXS) measurements were also performed to assess the packing motif/microstructure of neat and $C_{60}F_{48}$ -doped C_{16} IDT-BT layers (Figure 2d). The few diffraction peaks present in the 2D-GIWAXS patterns for the neat C_{16} IDT-BT and the corresponding in-plane and out-of-plane profiles (Figure S4, Supporting Information), indicate a low degree of structural order, in agreement with previous reports.^[22] Adding $C_{60}F_{48}$ in the C_{16} IDT-BT, at different concentrations, does not change the GIWAXS patterns (e.g., appearance of extra peaks or modification of existing ones), meaning that the microstructure of the C_{16} IDT-BT: $C_{60}F_{48}$ layers remain unaltered. The latter may prove advantageous for application in devices comprised of nanoscale channels, such as those formed via a-Lith (Figure 1d), where structural changes can prove detrimental.

Next, we investigated the potential of the neat and *p*-doped C_{16} IDT-BT as the active layer in Schottky diodes based on the asymmetric Au–Al planar electrodes shown in Figure 1c. Devices with empty nanogaps (i.e., without semiconductor) show very low current of $<10^{-10}$ A (Figure 3a) confirming the existence of an electrically isolating nanogap. Spin-coating the neat C_{16} IDT-BT on top of the Au–Al electrodes, results in devices with highly asymmetric current–voltage (*I*–*V*) characteristics with a rectification ratio of $\geq 10^3$ (Figure 3a). Under forward bias (negative potential applied on the Al electrode), holes are injected from the Au electrode and transported across the nanogap channel to recombine at the Al side. Evidently, doping of the C_{16} IDT-BT with $C_{60}F_{48}$ increases the diode's maximum forward current while shifting the V_{ON} toward 0 V. On the other hand, the diode's reverse current increases with increasing

$C_{60}F_{48}$ concentration, indicating increased carrier recombination at the junction. We attribute this to the presence of $C_{60}F_{48}$ and its deep LUMO (Figure 2b, inset) which could facilitate electron injection from the Au electrode and contribute to the recombination current.^[24] This hypothesis is supported by the increased dependence of the reverse current on the applied potential (1.5–2 V) seen in Figure 3a for 3 mol% $C_{60}F_{48}$. A small anticlockwise hysteresis is present in the *I*–*V* curves (Figure S5, Supporting Information) that appears to become prominent at higher $C_{60}F_{48}$ concentrations. This is most likely attributed to $C_{60}F_{48}$ -induced trap states.^[23] Importantly, the diode's forward current and rectification ratio can be tailored to a particular application without compromising its dark current by simply adjusting the nanogap width. This is illustrated in Figure 3b where scaling of the *W* in C_{16} IDT-BT: $C_{60}F_{48}$ (2.5 mol%) diodes leads to a tenfold increase of the maximum forward current while maintaining the reverse current low (<1 nA). Although the rectification ratio of our coplanar diodes are on par with previous published data ($\geq 10^4$) on organic diodes,^[15] the RC constants of our planar nanogap diodes are expected to remain significantly lower.

Next an equivalent-circuit model was developed to describe the planar C_{16} IDT-BT Schottky diodes using intrinsic and extrinsic components (Figure S6, Supporting Information). Such models are often used to emulate the actual parameters of Schottky diodes and are extremely useful for the design of more complex integrated circuits such as frequency mixers and voltage pumps.^[27] In our model the intrinsic part can be broken down into voltage-dependent junction capacitance (C_j), junction resistance (R_j), and series resistance (R_s). Unlike the vertical diode architecture (sandwich type), the planar diode configuration results in fewer extrinsic parasitic components. The air and substrate fringing fields generated across the

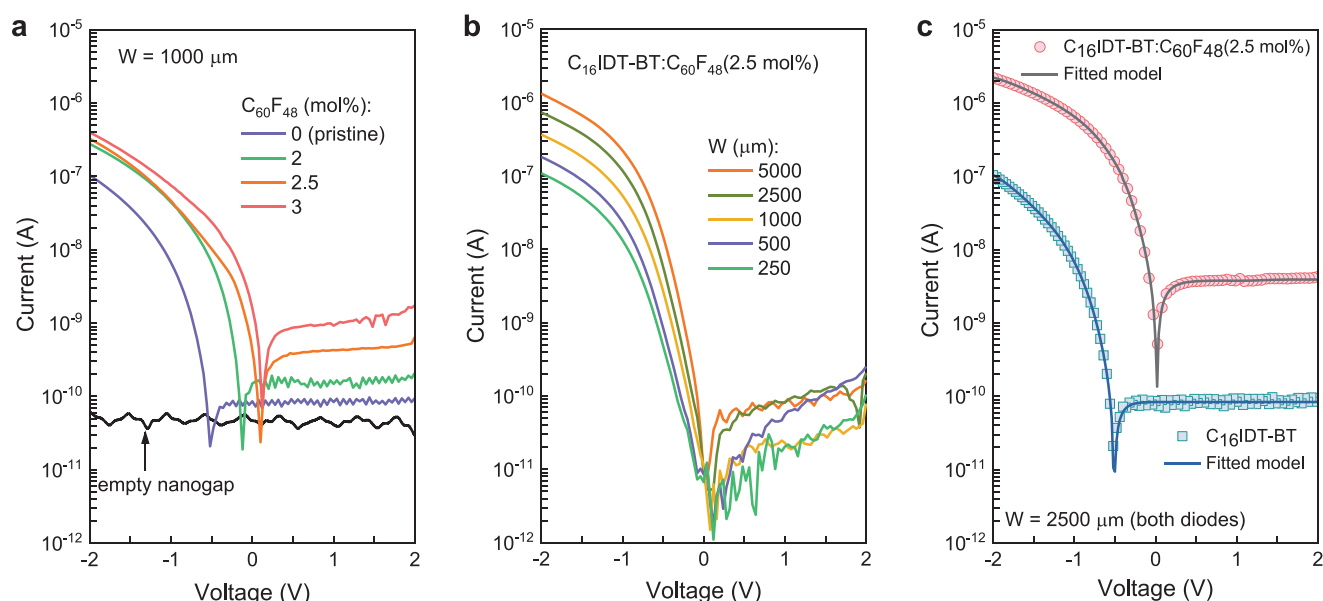


Figure 3. a) Current–voltage (*I*–*V*) characteristics of Al–Au nanogap diodes based on pristine C_{16} IDT-BT and $C_{60}F_{48}$ -doped C_{16} IDT-BT with different concentrations in the range 0–3 mol%. b) *I*–*V* characteristics of *p*-doped C_{16} IDT-BT: $C_{60}F_{48}$ (2.5 mol%) diodes with different channel widths (*W*) in the range 250–5000 μm . c) Experimental *I*–*V* curves (symbols) measured from pristine C_{16} IDT-BT and C_{16} IDT-BT: $C_{60}F_{48}$ (2.5 mol%) diodes fitted with the ADS model (solid lines). Both diodes in (c) had the same width (*W*) of 2500 μm .

junction perimeter are modeled as extrinsic parasitic fringing capacitance (C_p). The external parasitic capacitance (C_{pad}) and inductance (L_{pad}) between electrode and ground are negligible due to the good isolation from the external ground and small radial electrode dimensions. The thermionic field emission model that accounts for emission currents, as well as tunneling of electrons through the barrier, is used to extract the ideality factor (n) and the voltage-dependent series resistance (R_s) for neat and $C_{60}F_{48}$ -doped (2.5 mol%) C_{16} IDT-BT devices (Figure S7, Supporting Information). As summarized in Table S1 (Supporting Information), the voltage-dependent R_s is 2–3 orders of magnitude lower for the C_{16} IDT-BT: $C_{60}F_{48}$ (2.5 mol%) diode than the pristine one. Figure S8 (Supporting Information) shows the simplified advanced design software (ADS) model used for fitting the measured I – V curve while the comparison between measured (symbols) and modeled (lines) data is presented in Figure 3b. Overall, the ADS model based on the aforementioned equivalent circuit, was able to reproduce the measured I – V curves and can be seen as a valuable tool for the design of further circuitry.

To gain insights in the role of the p -dopant, we studied the evolution of the barrier height (Φ_b) in C_{16} IDT-BT diodes before and after doping with $C_{60}F_{48}$ (2.5 mol %), using capacitance–voltage (C – V) measurements. The latter is considered to be the most practical method for evaluating the Φ_b and the built-in potential (V_{bi}) in Schottky diodes.^[12] Figure S9a (Supporting Information) presents the C – V data for the neat C_{16} IDT-BT and p -doped C_{16} IDT-BT: $C_{60}F_{48}$ (2.5 mol%) diodes obtained at 1, 10, and 100 kHz. To improve the accuracy of our calculations, the extrinsic capacitances attributed to the 3D coupling of the planar nanogap electrode architecture and the glass substrate were estimated and appropriate corrections to the measured capacitance were applied using previously established protocols.^[12] The corrected Mott–Schottky plots obtained at 1 kHz for the C_{16} IDT-BT and C_{16} IDT-BT: $C_{60}F_{48}$ (2.5 mol%) diodes are shown in Figure S9b (Supporting Information). As expected, the Φ_b and V_{bi} for the C_{16} IDT-BT: $C_{60}F_{48}$ (2.5 mol%) diodes are significantly lower (0.6 and -0.4 V) than C_{16} IDT-BT diodes (1.6 and -1.4 V). The plateau observed in the near zero voltage region is attributed to shallow trap states induced by the molecular dopant.^[23,24] To better understand the contribution of each component on the diode operation, the total capacitance was modeled using

$$C_{total} = C_j + C_p = \frac{C_{j0}}{\sqrt{1 - \frac{V}{\Phi_{bi}}}} + C_p \quad (2)$$

where Φ_{bi} is built-in potential, C_{j0} is zero bias junction capacitance, and C_p accounts for parasitic capacitance due to the fringing fields present between the electrodes. The linear part of the experimentally determined $1/C^2$ versus V curve (Mott–Schottky plot) was then used as the curve-fitting region. We employed the Levenberg–Marquardt algorithm to fit Equation (2) to the measured C – V data in order to extract C_{j0} and C_p values (Figure S9c, Supporting Information) yielding 4.8×10^{-13} and 1.4×10^{-14} F, respectively, for neat C_{16} IDT-BT, and $\approx 9 \times 10^{-13}$ and $\approx 2.2 \times 10^{-14}$ F, respectively, for p -doped C_{16} IDT-BT: $C_{60}F_{48}$ (2.5 mol%) diodes. The slightly increase C_{j0} in

the latter is attributed to the narrowing of the depletion region width,^[28] and/or the increase of the accumulation region over larger parts of the electrodes near the nanogap region.

Next we looked into the high-frequency characteristics of our planar organic Schottky diodes. We note that as of to date there are only a handful of reports on organic Schottky diodes operating in the GHz frequency range. To the best of our knowledge, the work by Kang et al. on pentacene Schottky diodes operating at ≈ 1 GHz represents the best performance reported to-date.^[29] To evaluate the frequency response of our C_{16} IDT-BT planar diodes, one-port scattering parameter (S_{11}) measurements were used to extract the impedance and the intrinsic cutoff frequency ($f_{C-Int.}$) of the devices.^[30–32] The $f_{C-Int.}$ can be estimated from the intersection point of the real (Real R_s) and imaginary (Imag X_b) parts of the impedance curves shown in Figure 4a. Evidently, both pristine C_{16} IDT-BT and p -doped C_{16} IDT-BT: $C_{60}F_{48}$ (2.5 mol%) diodes with $W = 5000 \mu m$ exhibit intrinsic cutoff frequencies well above 1 GHz, clearly highlighting the advantage of the asymmetric nanogap architecture. The $f_{C-Int.}$ for the doped C_{16} IDT-BT: $C_{60}F_{48}$ (2.5 mol%) diodes is slightly higher (≈ 8 GHz) than for undoped C_{16} IDT-BT diodes (≈ 6 GHz), with both types of devices exhibiting a strong dependence on nanogap width, where a clear uptrend in $f_{C-Int.}$ with reducing W (Figure S10, Supporting Information), due to reduced C_j (Figure S11, Supporting Information), is observed. Importantly, the planar nanogap diodes are characterized by low capacitances of < 2 pF up to 10 GHz, making them ideal for high-frequency applications.

In order to explore the full potential of the technology, the extrinsic cutoff frequency ($f_{C-Ext.}$) of our planar diodes was determined experimentally using a rectifier circuit comprised of a tee bias and load resistor (Figure 4b) in the frequency range of 0.1–18 GHz. For simplicity, no matching circuit was used and as a result the actual power delivered to the diode is expected to be considerably lower than the nominal power outputted by the vector network analyzer (VNA) due to impedance mismatch. The $f_{C-Ext.}$ was extracted from the half-power point where the rectified DC voltage (V_{OUT}) drops to 0.707 of its initial maximum value.^[10,33] Though there is only a small difference in the extracted $f_{C-Ext.}$ between pristine C_{16} IDT-BT and p -doped C_{16} IDT-BT: $C_{60}F_{48}$ (2.5 mol%) diodes, the V_{OUT} increases by tenfold upon doping (Figure 4c). This major improvement is the result of favorable synergistic effects induced by the dopant and include: i) a reduced Φ_b , ii) a lower V_{bi} , and iii) a dramatically suppressed R_s (10^7 – $10^{10} \Omega$ for pristine vs 10^5 – $10^7 \Omega$ for p -doped devices, Table S1, Supporting Information). Interestingly, the DC V_{OUT} is found to scale with the diode's W (Figure 4d,e and Figure S12, Supporting Information) as well as with the nominal power of the input signal (Figure S13, Supporting Information). We attribute this to the improved impedance matching upon doping, which also highlights the possibility for further improvements. Increasing P_{in} to 17 dBm leads to diode breakdown followed by a sudden drop in V_{OUT} . The latter highlights the limitations on the power handling capabilities of these devices which is a consequence of their breakdown characteristics (Figure S14, Supporting Information). Despite this, however, the diodes should be well suited for low power applications such as energy harvesting circuits for IoT, and emerging telecommunication systems.^[34]

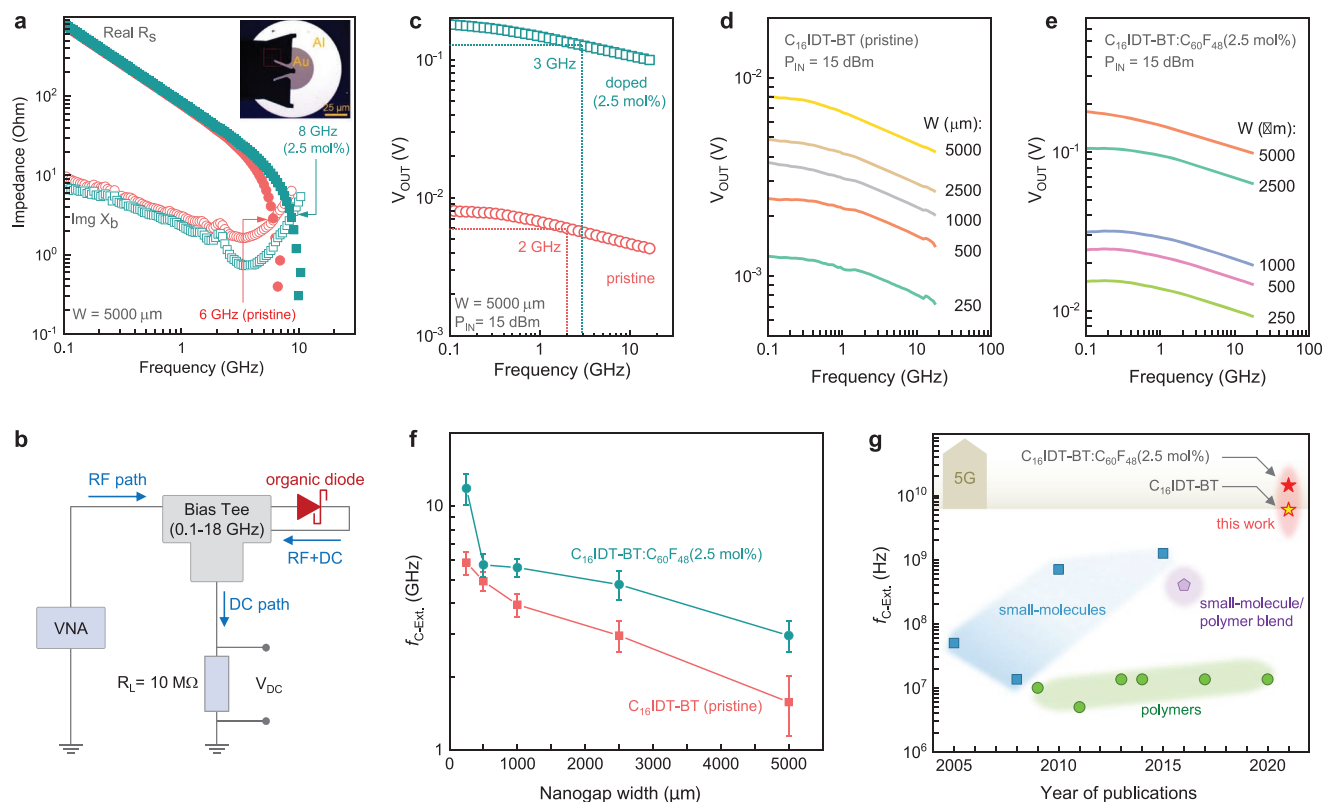


Figure 4. a) Frequency-dependent impedance of neat $C_{16}IDT-BT$ and $C_{16}IDT-BT:C_{60}F_{48}(2.5 \text{ mol}\%)$ polymer diodes with $W = 5000 \mu\text{m}$. b) Circuit diagram of the high-frequency rectifier measurement setup used. c) High-frequency rectified voltage output (V_{DC}) for neat and p -doped ($2.5 \text{ mol}\%$) $C_{16}IDT-BT$ polymer diodes with $W = 5000 \mu\text{m}$. d,e) Dependence of V_{OUT} on input signal frequency for neat $C_{16}IDT-BT$ and $C_{16}IDT-BT:C_{60}F_{48}(2.5 \text{ mol}\%)$ diodes of varying width (250, 500, 1000, 2500, and 5000 μm). f) Evolution of the calculated extrinsic cutoff frequency (f_{C-Ext}) for neat $C_{16}IDT-BT$ and $C_{16}IDT-BT:C_{60}F_{48}(2.5 \text{ mol}\%)$ diodes with the diodes width in the range 250–5000 μm . g) Reported f_{C-Ext} for various organic diodes over the past 20 years including this work.

The f_{C-Ext} for both $C_{16}IDT-BT$ and p -doped $C_{16}IDT-BT:C_{60}F_{48}(2.5 \text{ mol}\%)$ diodes increases with reducing W , due to lower capacitance, reaching an unprecedented maximum value of $\approx 14 \text{ GHz}$ for the 250 μm width p -doped diode (Figure 4f). The $I-V$ and RF performance of several devices manufactured on the same chip are also shown in Figure S15 (Supporting Information) and highlight the potential of a-Lith for the reliable manufacturing of organic RF electronics over large area substrates. However, one noticeable drawback is the sensitivity of the electrical performance of these coplanar diodes toward ambient atmosphere over time (Figure S16, Supporting Information). To this end, we anticipate significant improvements to be possible via encapsulation, and/or through the use of alternative organic semiconductors. For example, use of highly crystalline small molecule semiconductors that combine high carrier mobility with ambient stability could lead to significant performance boost. Despite this issue the level of performance of our organic Schottky diodes surpasses all previously published data, clearly highlighting the tremendous advantage of the planar nanogap architecture. This is better illustrated in Figure 4g where the f_{C-Ext} of best-performing organic Schottky diodes reported to date are summarized. In this plot one can clearly see the large upward jump in performance enabled by our planar nanogap

$C_{16}IDT-BT$ diodes, placing them well within the 5G frequency spectrum for the first time.

3. Conclusion

In summary, we have shown that combining asymmetric self-aligned nanogap electrodes patterned by a-Lith with the high mobility organic polymer $C_{16}IDT-BT$, enables the development of the first organic Schottky diodes operating within the 5G frequency spectrum. Molecular doping of the polymer semiconductor was used to enhance the performance of the diodes highlighting the potential for further improvements. For example, use of suitable self-assembled monolayers (SAMs) as electrode work function modifiers could be explored to lower the contact resistance further and increase both the f_{C-Ext} and V_{OUT} . Similar improvements could be anticipated through the use of organic semiconductors with higher mobility,^[40] and/or improved doping schemes.^[41] Overall, our approach addresses inherent limitations associated with conventional organic Schottky diodes and paves the way to further research toward cost-effective RF electronics. We expect that the simplicity, large-area compatibility, and possibility for monolithic integration of our organic diodes with antennas and other passive and

active components, makes them an attractive technology for application in wireless energy harvesting and telecommunications in the forthcoming IoT era.

4. Experimental Section

Adhesion Lithography for Nanogap Electrode Fabrication: Thermally evaporated Aluminum (Al) films were patterned on Borofloat glass substrates using conventional photolithography via bright field patterning and wet chemical etching. The patterned substrates were immersed in 1×10^{-3} M (7.8 mg of octadecylphosphonic acid in 30 mL of isopropyl alcohol) solution for 20 h to allow the formation of self-assembled monolayer (SAM) on Al (M1 electrode). The substrates were rinsed with isopropyl alcohol to ensure the removal of physisorbed SAM on the substrates then dried at 80 °C in air on a hotplate for 15 min. Next, a 5/95 nm thick Al/Au film (M2 electrode) was evaporated on top of the entire substrate. The 5 nm of Al was used to promote the adhesion between the Au electrode and the substrate. Due to the reduced adhesion between M2 and M1/SAM, the selective removal of M2 was achieved by applying a glue (first contact) to the surface of the sample followed by a mechanical peel-off step. The selective removal of the overlapping M2 causes the formation of a nanogap between M1 and M2. The SAM atop M1 was then removed by 2 min of Ar plasma treatment prior to the semiconductor layer deposition.

Material Preparation: C_{16} DT-BT (M_n 65 kg mol $^{-1}$ with a dispersity (\bar{D}) of 2.42 as measured by GPC in chlorobenzene at 80 °C against polystyrene standards) and $C_{60}F_{48}$ were synthesized using previously reported procedures.^[35,36] Anhydrous chlorobenzene (CB) and 1,2-dichlorobenzene (oDCB) was purchased from Sigma-Aldrich and used as received. Solutions of C_{16} DT-BT (5 mg mL $^{-1}$ in oDCB) were prepared and stirred overnight at 100 °C, while solutions of $C_{60}F_{48}$ (1 mg mL $^{-1}$ in CB) were stirred overnight at room temperature. The dopant solution was then added to the semiconductor solution in order to obtain the required concentration, which was calculated in mol% of the dopant in respect to the molecular weight of one monomer of the polymer. Doped solutions were then stirred for 2 h at room temperature and spin-coated at 1000 rpm for 60 s, followed by an annealing treatment of 2 min to remove the excess of solvent. The entire process was carried out in a nitrogen-filled glove box.

Scanning Electron Microscope (SEM): The SEM topology images of Al/Au nanogap electrodes were acquired by an ultrahigh resolution field emission Magellan SEM equipped with two-mode final lens (immersion and field-free). The high resolution images were obtained using the immersion mode at 5–10 kV after appropriate beam and lens alignments.

UV-Vis Absorption Spectroscopy: Absorption spectra were measured with a Shimadzu UV-2600 spectrophotometer.

Kelvin-Probe Work-Function Measurement: Work function measurements of pristine and *p*-doped C_{16} DT-BT films were carried out using the Kelvin Probe technique using a KP Technology SPS040 system. Samples were prepared by depositing polymer films with doping concentrations between 0 and 5 mol% on top of ITO covered glass slides. As reference material, a freshly cleaned highly oriented pyrolytic graphite (HOPG) film with an expected work function of ≈ 4.5 eV was used. Since this reference value for HOPG was not measured directly, the actual values given in Figure 2b might be subject to small, but systematic, deviation. As such this work expects that the progression of work function changes due to increased dopant concentration to remain the same, regardless of the absolute value of the reference HOPG. To minimize unwanted effects (e.g., adsorption of water and oxygen), all measurements were carried out inside a dry nitrogen filled glove box.

Grazing Incidence Wide Angle X-Ray Scattering (GIWAXS): Diffraction patterns at grazing incidence were taken at the BL11, NCD-SWEET, beamline at ALBA Synchrotron, Cerdanyola del Vallès (Spain). The energy beam was set at 12.4 keV ($\lambda = 0.1$ nm) using a channel cut Si (1 1 1) monochromator. The incident angle was set at 0.12° and the exposition time was 5 s. GIWAXS patterns were taken with a Rayonix

LX255-HS area detector (pixel size of 88 microns), placed at 210 mm from the sample position. 2D-GIWAXS patterns were corrected as a function of the components of the scattering vector with a Matlab script developed by Aurora Nogales and Edgar Gutiérrez [https://it.mathworks.com/matlabcentral/fileexchange/71958-grazing-incidence-wide-angle-x-ray-scattering-representation]. Material solutions were prepared and processed following the same procedures used for the device fabrication on top of silicon substrates.

Organic Transistors Fabrication and Characterization: OTFTs were fabricated with a top-gate, bottom-contact (TG-BC) architecture onto 2.54×2.54 cm 2 glass substrates. The source/drain electrodes composed of Al/Au (5/35 nm) were defined with shadow masks via thermal evaporation. The substrates were then cleaned by sonication in acetone and isopropanol, followed by an Argon plasma treatment for 2 min. Pristine and $C_{60}F_{48}$ -doped C_{16} DT-BT solutions were prepared and spin-coated on top of the substrates following the same procedures employed for the nanogap diodes fabrication (i.e., 1000 rpm for 60 s at RT), followed by an annealing step at 100 °C for 2 min. Cytop, acting as the gate dielectric, was then spin-coated atop the organic layer at 4000 rpm for 90 s (thickness ≈ 600 nm) and annealed at 80 °C for 1 h. The Al gate electrode was then thermally evaporated through a shadow mask. Finally, the devices were transferred to the measurement setup inside a nitrogen-filled glove box using a transfer tube. Electrical characterization was performed with an Agilent B2902A semiconductor parameter analyzer.

Diode Characterization: The current–voltage (*I*–*V*) characteristics of the diodes were measured using Keysight B2912A precision sourcemeter. The capacitance measurements were performed using a Keysight B1500A semiconductor device analyzer. All electrical measurements were carried out inside a nitrogen-filled glove box.

Radio Frequency Measurements: The one-port scattering parameter (S_{11}) measurements in the frequency range 0.01–50 GHz were measured in ambient conditions using an Agilent Network analyzer (PNA N5225A) connected to a Cascade Microtech probe station. Cascade Infinity GSG probes (ACP-40) having a pitch of 250 μ m were used with the valid Open, Short and Load (OSL) calibration on impedance standard substrate (ISS) of 106–682. The rectifier circuit measurements were carried out inside the nitrogen-filled glove box using tee bias (0.1 MHz–18 GHz, from Pasternack), a 10 M Ω load resistor, and a Keysight 34465A digital multimeter.

Supporting Information

Supporting Information is available from the Wiley Online Library or from the author.

Acknowledgements

K.L. and A.D.S. contributed equally to this work. This publication was based upon work supported by the King Abdullah University of Science and Technology (KAUST), KAUST Solar Centre Office of Sponsored Research (OSR) under Award Nos. OSR-2018-CARF/CCF-3079, OSR-2019-CRG8-4095.3, and OSR-2020-CRG9-4347.

Conflict of Interest

The authors declare no conflict of interest.

Data Availability Statement

The data that support the findings of this study are available from the corresponding author upon reasonable request.

Keywords

organic semiconductor, printed electronics, radio frequency electronics, rectifier circuits, Schottky diodes

Received: October 23, 2021
Revised: December 16, 2021
Published online:

- [1] J. Semple, D. G. Georgiadou, G. Wyatt-Moon, G. Gelinck, T. D. Anthopoulos, *Semicond. Sci. Technol.* **2017**, 32, 123002.
- [2] S. Dang, O. Amin, B. Shihada, M.-S. Alouini, *Nat. Electron.* **2020**, 3, 20.
- [3] S. Kim, R. Vyas, J. Bito, K. Niotaki, A. Collado, A. Georgiadis, M. M. Tentzeris, *Proc. IEEE* **2014**, 102, 1649.
- [4] M. Cansiz, D. Altinel, G. K. Kurt, *Energy* **2019**, 174, 292.
- [5] C. R. Valenta, G. D. Durgin, *IEEE Microwave Mag.* **2014**, 15, 108.
- [6] Y. Chu, C. Qian, P. Chahal, C. Cao, *Adv. Sci.* **2019**, 6, 1801653.
- [7] U. Zschieschang, J. W. Borchert, M. Giorgio, M. Caironi, F. Letzkus, J. N. Burghartz, U. Waizmann, J. Weis, S. Ludwigs, H. Klauk, *Adv. Funct. Mater.* **2019**, 30, 1903812.
- [8] D. J. Beesley, J. Semple, L. Krishnan Jagadamma, A. Amassian, M. A. McLachlan, T. D. Anthopoulos, J. C. deMello, *Nat. Commun.* **2014**, 5, 3933.
- [9] W.-Y. Uhm, S.-G. Choi, M. Han, K.-K. Ryu, S.-C. Kim, *J. Electr. Eng. Technol.* **2016**, 11, 1367.
- [10] D. G. Georgiadou, J. Semple, A. A. Sagade, H. Forstén, P. Rantakari, Y.-H. Lin, F. Alkhalil, A. Seikhan, K. Loganathan, H. Faber, T. D. Anthopoulos, *Nat. Electron.* **2020**, 3, 718.
- [11] J. Semple, S. Rossbauer, C. H. Burgess, K. Zhao, L. K. Jagadamma, A. Amassian, M. A. McLachlan, T. D. Anthopoulos, *Small* **2016**, 12, 1993.
- [12] J. Semple, S. Rossbauer, T. D. Anthopoulos, *ACS Appl. Mater. Interfaces* **2016**, 8, 23167.
- [13] S. Kano, T. Kawazu, A. Yamazaki, M. Fujii, *Nanotechnology* **2019**, 30, 285303.
- [14] A. Basu, M. R. Niazi, A. D. Scaccabarozzi, H. Faber, Z. Fei, D. H. Anjum, A. F. Paterson, O. Boltalina, M. Heeney, T. D. Anthopoulos, *J. Mater. Chem. C* **2020**, 8, 15368.
- [15] M. Cao, W. J. Hyun, L. F. Francis, C. D. Frisbie, *Flexible Printed Electron.* **2020**, 5, 015006.
- [16] A. M. Zeidell, D. S. Filston, M. Waldrip, H. F. Iqbal, H. Chen, I. McCulloch, O. D. Jurchescu, *Adv. Mater. Technol.* **2020**, 5, 2000390.
- [17] J. Yang, Z. Zhao, S. Wang, Y. Guo, Y. Liu, *Chem* **2018**, 4, 2748.
- [18] M. Nikolka, I. Nasrallah, B. Rose, M. K. Ravva, K. Broch, A. Sadhanala, D. Harkin, J. Charmet, M. Hurhangee, A. Brown, S. Illig, P. Too, J. Jongman, I. McCulloch, J. L. Bredas, H. Sirringhaus, *Nat. Mater.* **2017**, 16, 356.
- [19] Z. A. Lampart, K. J. Barth, H. Lee, E. Gann, S. Engmann, H. Chen, M. Guthold, I. McCulloch, J. E. Anthony, L. J. Richter, D. M. DeLongchamp, O. D. Jurchescu, *Nat. Commun.* **2018**, 9, 5130.
- [20] D. Venkateshvaran, M. Nikolka, A. Sadhanala, V. Lemaire, M. Zelazny, M. Kepa, M. Hurhangee, A. J. Kronemeijer, V. Pecunia, I. Nasrallah, I. Romanov, K. Broch, I. McCulloch, D. Emin, Y. Olivier, J. Cornil, D. Beljonne, H. Sirringhaus, *Nature* **2014**, 515, 384.
- [21] A. Wadsworth, H. Chen, K. J. Thorley, C. Cendra, M. Nikolka, H. Bristow, M. Moser, A. Salleo, T. D. Anthopoulos, H. Sirringhaus, I. McCulloch, *J. Am. Chem. Soc.* **2020**, 142, 652.
- [22] X. Zhang, H. Bronstein, A. J. Kronemeijer, J. Smith, Y. Kim, R. J. Kline, L. J. Richter, T. D. Anthopoulos, H. Sirringhaus, K. Song, M. Heeney, W. Zhang, I. McCulloch, D. M. DeLongchamp, *Nat. Commun.* **2013**, 4, 2238.
- [23] A. F. Paterson, N. D. Treat, W. Zhang, Z. Fei, G. Wyatt-Moon, H. Faber, G. Vourlias, P. A. Patsalas, O. Solomeshch, N. Tessler, M. Heeney, T. D. Anthopoulos, *Adv. Mater.* **2016**, 28, 7791.
- [24] A. F. Paterson, Y.-H. Lin, A. D. Mottram, Z. Fei, M. R. Niazi, A. R. Kirmani, A. Amassian, O. Solomeshch, N. Tessler, M. Heeney, T. D. Anthopoulos, *Adv. Electron. Mater.* **2018**, 4, 1700464.
- [25] A. D. Scaccabarozzi, F. Scuratti, A. J. Barker, A. Basu, A. F. Paterson, Z. Fei, O. Solomeshch, A. Petrozza, N. Tessler, M. Heeney, T. D. Anthopoulos, M. Caironi, *Adv. Electron. Mater.* **2020**, 6, 2000539.
- [26] I. E. Jacobs, A. J. Moule, *Adv. Mater.* **2017**, 29, 1703063.
- [27] A. Y. Tang, V. Drakinskiy, K. Yhland, J. Stenarson, T. Bryllert, J. Stake, *IEEE Trans. Microwave Theory Tech.* **2013**, 61, 1870.
- [28] S. M. N. Sze, K. Kwok, *Physics of Semiconductor Devices*, 3rd Ed., John Wiley & Sons, Inc., **2007**.
- [29] C.-m. Kang, J. Wade, S. Yun, J. Lim, H. Cho, J. Roh, H. Lee, S. Nam, D. D. C. Bradley, J.-S. Kim, C. Lee, *Adv. Electron. Mater.* **2016**, 2, 1500282.
- [30] J. Zhang, Y. Li, B. Zhang, H. Wang, Q. Xin, A. Song, *Nat. Commun.* **2015**, 6, 7561.
- [31] J. Zhang, H. Wang, J. Wilson, X. Ma, J. Jin, A. Song, *IEEE Electron Device Lett.* **2016**, 37, 389.
- [32] S. J. Yang, K. T. Park, J. Im, S. Hong, Y. Lee, B. W. Min, K. Kim, S. Im, *Nat. Commun.* **2020**, 11, 1574.
- [33] X. Zhang, J. Grajal, J. L. Vazquez-Roy, U. Radhakrishna, X. Wang, W. Chern, L. Zhou, Y. Lin, P. C. Shen, X. Ji, X. Ling, A. Zubair, Y. Zhang, H. Wang, M. Dubey, J. Kong, M. Dresselhaus, T. Palacios, *Nature* **2019**, 566, 368.
- [34] X. Zhang, J. Grajal, M. López-Vallejo, E. McVay, T. Palacios, *Joule* **2020**, 4, 1148.
- [35] W. Zhang, J. Smith, S. E. Watkins, R. Gysel, M. McGehee, A. Salleo, J. Kirkpatrick, S. Ashraf, T. Anthopoulos, M. Heeney, I. McCulloch, *J. Am. Chem. Soc.* **2010**, 132, 11437.
- [36] A. V. Kepman, V. F. Sukhovikhov, A. Tressaud, C. Labrugere, E. Durand, N. S. Chilingarov, L. N. Sidorov, *J. Fluorine Chem.* **2006**, 127, 832.
- [37] Y. Smets, C. B. Stark, F. Schmitt, M. T. Edmonds, S. Lach, C. A. Wright, D. P. Langley, K. J. Rietwyk, A. Schenk, A. Tadich, M. Wanke, C. Ziegler, L. Ley, C. I. Pakes, *Org. Electron.* **2013**, 14, 169.
- [38] M. T. Edmonds, M. Wanke, A. Tadich, H. M. Vulling, K. J. Rietwyk, P. L. Sharp, C. B. Stark, Y. Smets, A. Schenk, Q. H. Wu, L. Ley, C. I. Pakes, *J. Chem. Phys.* **2012**, 136, 124701.
- [39] K. J. Rietwyk, M. Wanke, H. M. Vulling, M. T. Edmonds, P. L. Sharp, Y. Smets, Q. H. Wu, A. Tadich, S. Rubanov, P. J. Moriarty, L. Ley, C. I. Pakes, *Phys. Rev. B* **2011**, 84, 035404.
- [40] A. F. Paterson, S. Singh, K. J. Fallon, T. Hodsdon, Y. Han, B. C. Schroeder, H. Bronstein, M. Heeney, I. McCulloch, T. D. Anthopoulos, *Adv. Mater.* **2018**, 30, 1801079.
- [41] A. D. Scaccabarozzi, A. Basu, F. Aniés, J. Liu, O. Zapata-Arteaga, R. Warren, Y. Firdaus, M. I. Nugraha, Y. Lin, M. Campoy-Quiles, N. Koch, C. Müller, L. Tsetseris, M. Heeney, T. D. Anthopoulos, *Chem. Rev.* **2021**, <https://doi.org/10.1021/acs.chemrev.1c00581>.